ACS APPLIED NANO MATERIALS

www.acsanm.org Article

Combinatorial Printing of Iron and Cobalt Reactive Inks to Produce Magnetic Amorphous and Nanocrystalline Metals

Collin E. Miller, Joshua Edwards, Chris Matsumura, Matthew Michael Schneider, Serena Eley, Suveen N. Mathaudhu, and Owen J. Hildreth*

Cite This: https://doi.org/10.1021/acsanm.4c05047 Read Online

ACCESS | Metrics & More | Article Recommendations | Supporting Information

ABSTRACT: Reactive inks are an attractive method to selectively pattern metallic features with minimal post-processing. While significant progress has been made developing silver and copper reactive inks for printed electronics, less progress has been made in developing metal reactive inks with properties suitable for structural or magnetic applications. To address this gap, this work introduces particle-free iron and cobalt metal reactive inks to print magnetic iron and cobalt metals. Interestingly, structure analysis of the printed reactive inks showed that the iron reactive ink produced fully amorphous iron and the cobalt reactive ink produced nanocrystals dispersed in an amorphous matrix. This work also demonstrates two combinatorial methods of printing these inks: by mixing the two inks together to produce amorphous iron−cobalt alloys and by spatially patterning the iron and cobalt monometallic inks to achieve control over both the local composition and the correlated atomic structure. Triiron dodecacarbonyl and dicobalt octacarbonyl are used as the iron and cobalt metal precursors, respectively, because these zerovalent metal complexes directly decompose to metal and carbon monoxide gas. The printed metals' elemental and chemical compositions were evaluated using energy dispersive X-ray spectroscopy, X-ray photoelectron spectroscopy, and Mössbauer effect spectroscopy showing that the amorphous phases are likely stabilized by either remnant carbonyl bonds from incomplete decomposition of the metal carbonyl or residual octylamine solvent interacting with the metal atoms. Additional characterization includes resistivity measurements to verify metallic conductivity, nanoindentation to quantify hardness, and magnetometry studies to quantify the magnetic performance. As a demonstration, the Fe and Co reactive inks were sequentially printed in a combinatorial layer-by-layer manner to produce a vertically graded iron and cobalt line, as well as a matrix of nanocrystalline cobalt dots on an amorphous iron film. Overall, this work introduces a method to directly print continuous, amorphous, magnetic, and structural alloys at moderate temperatures from a particle-free reactive ink.

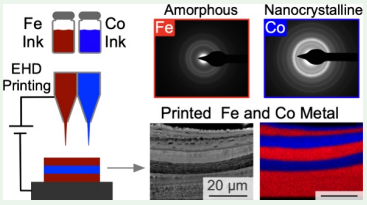

KEYWORDS: *amorphous metal, additive manufacturing, reactive ink, metal organic decomposition ink, nanocrystalline, electrohydrodynamic*

INTRODUCTION

Particle-free reactive inks enable precise and selective deposition of metallic features and structures with high spatial resolution and minimal post-processing, promising the ability to manufacture high-quality devices at low cost.[1,2] Unlike traditional, particle-based inks that effectively print clusters of particles, reactive inks print chemical reactions that precipitate the desired material at reasonably low temperatures, typically on the order of 23 to 300 °C.[3,4] The field of reactive inks has grown significantly over the past decade; however, ink development has largely focused on printing conductive materials for printed electronics.[5,6] While there has been some work printing nickel reactive inks to deposit magnetic materials,[7] it is important to develop new reactive ink systems for a wide range of functional materials to print optical, structural, and magnetic components.[8−10] Development of iron and cobalt reactive inks with good magnetic properties[11−13] could expand the types of materials and devices that can be manufactured using reactive inks, such as inductors,[14] magnetic sensors,[10] and magnetic actuators.[15] This work introduces a novel, particle-free reactive ink system capable of printing and patterning continuous magnetic amorphous iron and nanoparticle cobalt with spatial control over both local composition and, through composition, local atomic structure. These results were achieved at moderate temperatures (190 °C) and without post-processing. This is important because, to date, iron inks relied on nanoparticles, which are either left as nanoparticle composites or required sintering temperatures greater than 600 °C to produce continuous metallic material.[15,16]

Numerous classes of metal reactive inks exist depending on the type of reaction mechanisms and conditions used to precipitate the target material. This includes self-reducing inks, where the ink contains reducing agents so that the metal

Received: September 2, 2024
Revised: November 11, 2024
Accepted: November 13, 2024

https://doi.org/10.1021/acsanm.4c05047
ACS Appl. Nano Mater. XXXX, XXX, XXX−XXX

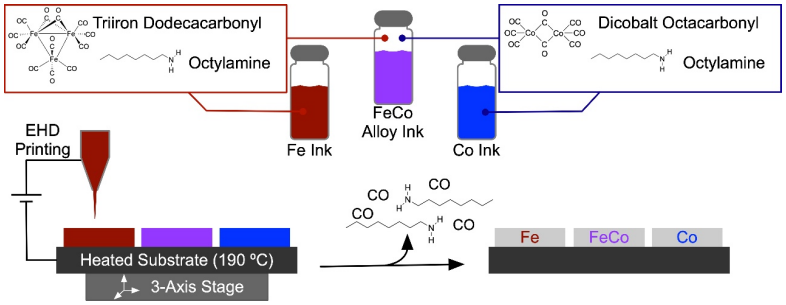

Figure 1. Schematic of the three different metal-carbonyl-based MOD inks investigated in this study. The monometallic iron or cobalt ink is made from triiron dodecacarbonyl or dicobalt octacarbonyl, respectively, which is dissolved in octylamine. The iron−cobalt ink that produces a FeCo alloy is made from both metal carbonyls dissolved in octylamine. The inks are deposited with an electrohydrodamic printer onto a substrate heated to 190 °C, which decomposes the metal carbonyl to metal and carbon monoxide and vaporizes the octylamine solvent.

cations can be reduced at lower processing temperatures;[17] postreduction inks, where the inks are exposed to a reducing agent after deposition;[18] electrohydrodynamic redox inks, where the applied electric potential used in electrohydrodynamic printing preferentially eject metal cations that are subsequently reduced on the printed surface through charge-transfer from the substrate;[19] and metal−organic decomposition (MOD) inks, where organometallic precursors are decomposed to metal through radiation such as thermal,[4] plasma,[20] or laser.[21] These different inks are compatible with numerous patterning methods that have varying resolutions, throughputs, and processable viscosities. Some proven methods include inkjet printing,[22] aerosol jet printing,[23] contact dispense printing,[2] and electrohydrodynamic (EHD) printing.[24]

This work focuses on EHD printing of MOD inks to print iron and cobalt metals at reasonably low temperatures. EHD printing was chosen for a couple of reasons. First, the tunable gap between the substrate and printhead (stand-off distance) keeps the nozzle cool even when printing onto heated substrates for in situ decomposition, which eliminates the need for post processing. Second, EHD printing works with a wide range of ink viscosities and surface tensions[25] and is reasonably scalable,[26] with some groups demonstrating parallel printing through multiple tips.[19] Figure 1 schematically illustrates the three iron and cobalt MOD inks used in this work along with the EHD printing setup. For the MOD inks, triiron dodecacarbonyl and dicobalt octacarbonyl were selected as organometallic precursors and dissolved in octylamine. These zerovalent metal carbonyls are particularly attractive because they thermally decompose to precipitate solid Fe or Co while the carbonyl ligands are released as carbon monoxide gas.

Traditionally, metal carbonyls are used to produce metal nanoparticles or high purity metal powders.[27−30] This work shows that metal carbonyl inks containing triiron dodecacarbonyl can also be used to print continuous amorphous metals. Amorphous metals are solid metallic materials lacking long-range order. Due to their noncrystalline structure, amorphous metals often exhibit remarkable properties, such as high strength,[31] corrosion resistance,[32] and unique magnetic properties.[12] The random arrangement of atoms that provide these benefits are configurationally frozen in a metastable state and often require rapid quenching from a melt in order to overcome the large driving force for crystallization inherent to many metallic systems.[33,34] Amorphous metals are traditionally produced using rapid quench techniques;[35−38] however, other methods such as mechanical,[39] ion irradiation,[40] and chemical[41] have been used to make amorphous metals.

The amorphous metal produced by this work's metal carbonyl inks follows the chemical route. Traditionally, chemical methods of producing amorphous metals typically result in particles that require further processing to form a solid film or a 3D structure. A couple examples of chemically produced amorphous particles are the synthesis of amorphous iron boride nanoparticles through the reduction of iron(II) chloride with sodium borohydride[42] and iron pentacarbonyl decomposed using a number of techniques (including electrical discharge,[43] sonochemical,[44] and thermal[30]). To manufacture a solid part from traditional chemically synthesized amorphous metals, post processing steps would be required such as selective laser melting (SLM)[38] or powder metallurgy (sintering)[45,46] to join amorphous particles. Reactive inks represent a novel chemical-based route of producing continuous amorphous metal in situ without needing post-processing steps. This new ability to directly print continuous amorphous metals without requiring a mix of fast cooling rates, complex alloy elements, or quenching from a melt should enable the integration of this unique material state into advanced printed devices.

For this work, the atomic structure of the printed metal carbonyl inks was characterized using X-ray diffraction (XRD) and transmission electron microscopy (TEM) to show that the iron and iron−cobalt alloy were amorphous, while the printed cobalt produced oblong nanoparticles embedded in an amorphous matrix. This provides a useful opportunity to highlight the spatial control over deposition and the combinatorial benefits afforded by ink-based printing. Printed alloys can be made by mixing different combinations of inks or ink components and then depositing them;[47] or functionally graded materials can be produced by precisely depositing combinations of inks.[23,48] The inks in this work are used to print both iron−cobalt alloys from a single ink and print graded layers of amorphous iron and nanocrystalline cobalt using two different inks. Additionally, lateral control over composition and crystallinity is also demonstrated by printing an array of nanocrystalline cobalt on an amorphous iron film. Additional characterization of the composition and mechanical and magnetic properties of the fabricated metal prints was performed. Nanoindentation studies on the dense, printed iron samples showed that the hardness of the printed iron was 3.9 GPa, which is very similar to annealed pure iron (~3.7 GPa) but low for an amorphous metal.[49] Magnetometry studies revealed that the magnetic saturation and coercivity of the

https://doi.org/10.1021/acsanm.4c05047
ACS Appl. Nano Mater. XXXX, XXX, XXX−XXX

printed iron is 89 emu/g and 90 Oe, respectively, which is comparable to previously synthesized amorphous iron nanoparticles.[29] Lastly, iron lines and films were directly printed onto polyimide tape using the iron reactive ink to demonstrate the ability to print continuous metals on temperature sensitive substrates (Figure S11).

Overall, this work expands the types of materials that can be produced from reactive inks by printing magnetic, amorphous, transition metals and spatially controlled composites. Each one of these aspects has potential applications, making these inks truly multifunctional. For example, particle free iron inks could replace traditional, sacrificial polymer binders used in binder jet printing to bind metal powders and produce a green part without post processing. The work by Yoo used iron nanoparticle inks to bind steel powder and still required a 600 °C postprint sintering step to produce a fragile green part.[16] Hypothetically, a reactive iron ink could replace both the nanoparticle/dispersant and the high temperature postprint sintering step. The magnetic properties of our Fe/Co reactive inks make them well suited to being integrated into printed magnetic devices and actuators. Whereas current efforts rely on printed magnetic polymer composites which have a lower magnetic saturation of 5 emu/g,[15] our FeCo alloy reactive ink has a magnetic saturation of 94 emu/g. Additionally, this work illustrates the combinatorial printing of the individual Fe and Co reactive inks to demonstrate discrete spatial control over local composition. The spatial control over crystallinity (by switching between the amorphous-producing Fe ink and the nanoparticle-producing Co ink) enabled by these new inks could be used to study high-impact energy shock absorbers that rely on layered amorphous and crystalline layers, which are currently manufactured using multiple processing steps to form each layer.[34,50] Overall, this facile printing method provides a new route to produce amorphous and magnetic materials for a broad range of applications ranging from device fabrication to structural and mechanical uses.

EXPERIMENTAL METHODS

Materials. The Fe and Co MOD reactive inks used in this work were formulated by dissolving triiron dodecacarbonyl ($Fe_3(CO)_{12}$) or dicobalt octacarbonyl ($Co_2(CO)_8$) in octylamine. All chemicals were sourced from Sigma-Aldrich and were used as received without further purification. Triiron dodecacarbonyl was chosen over iron pentacarbonyl because its decomposition temperature is lower than its boiling point while also being less volatile and toxic.[28]

Preliminary solvent and temperature studies (shown in Figure S1) were conducted for the iron ink using heptylamine and octylamine as solvents. Printing at 190 °C produced the densest iron lines when printing at temperatures ranging from 160 to 190 °C. Octylamine was selected as a suitable solvent because it balanced fast solvent evaporation and suppression of the Leidenfrost effect at the optimized 190 °C printing temperature. This is important because solvents with boiling points significantly below the printing temperature suffered from the Leidenfrost effect, making it difficult to build a continuous structure. Solvents with boiling temperatures significantly above the printing temperature evaporated too slowly to print in a continuous manner. Overall, our preliminary studies found that octylamine balanced the need for rapid evaporation while avoiding the Leidenfrost effect.

Ink Synthesis. All ink synthesis and printing were conducted in a VAC-ATM Omni-Lab glovebox with a nitrogen environment nominally purified with a built-in purifier. The atmosphere maintained an oxygen concentration below 5 ppm and a water concentration below 20 ppm during synthesis and printing, as measured using the detectors built into the glovebox. Additionally, a set of VAC-ATM Genesis oxygen and water purifiers were placed in the glovebox and run during the printing process to capture any reaction products entering the atmosphere.

The iron carbonyl MOD inks were synthesized by dissolving 0.14 g of triiron dodecacarbonyl in 1.8 mL of octylamine in a 1 dram glass vial. The mixture is stirred with a magnetic stir bar for approximately 30 min, during which the solution becomes a blood-red color and increases in viscosity. The cobalt carbonyl MOD inks were synthesized by dissolving 0.1 g of dicobalt octacarbonyl in 1.8 mL of octylamine in a 1 dram glass vial. A white vapor was observed coming out of the vial as the dicobalt octacarbonyl was added. The mixture is stirred for approximately 30 min, during which the solution becomes a red wine color that is more translucent than the iron ink with some precipitation observed. This precipitate was separated out of the ink immediately before printing using the process described in the following paragraph. The FeCo alloy ink was synthesized by first dissolving 0.14 g of triiron dodecacarbonyl in octylamine. The mixture is stirred for approximately 10 min and then 0.08 g of dicobalt octacarbonyl is dissolved into the solution. The resulting solution is stirred for another 30 min.

All inks were synthesized on the same day as the printing process. Additionally, solid particles were observed in the inks after synthesis. Particles were removed immediately before printing by centrifuging the inks at 4000 rpm for 30 min with the supernatant carefully removed using a glass pipet and then used as the ink. The mass of the particles collected from the iron ink was 0.002 g. An ink stability study was conducted, and no additional particles were collected after stirring the iron ink for 72 h and centrifuging it again. The mass of the particles collected from the cobalt ink was 0.004 g. The monometallic cobalt ink visibly precipitated material; however, the composition of the precipitate was not determined. After stirring the cobalt ink for 72 h and centrifuging again, 0.003 g of precipitate was collected. The 1:1 Fe:Co ink was too dark to see any precipitate form; however, solid particles were present after centrifugation. It was not determined if they came from the Fe or Co precursors or a mix of the two.

The three inks studied in this work and described above were printed using the three inks in Table 1. As shown in Table 1, the concentration of iron and cobalt in the FeCo alloy ink does not match the final printed composition; this is due to incomplete solvation and particle precipitation. Table S1 lists the at % of Fe and Co in the final prints as determined using EDS. It also includes two additional inks that were printed to determine the appropriate ratio of Fe to Co to achieve 50:50 prints, as well as demonstrate the ability to tune alloy composition.

Table 1. Iron and Cobalt Concentration in Each Ink vs the Printed Ratio with at % O Impurity Quantified Using EDS

name	Fe (mol/L)	Co (mol/L)	printed ratio (Fe:Co)	O impurity (at %)
Fe	0.28	0.00	1:0	8
Co	0.00	0.20	0:1	8
FeCo alloy	0.28	0.16	1:1 (measured 49:51)	6

Printing. Printing was conducted using a custom-built electrohydrodynamic (EHD) printer. EHD printing was selected because the gap between the substrate and print head (stand-off distance) allows the printhead to be cooler than the substrate, which helps prevent premature ink decomposition and nozzle clogging. Additionally, EHD printing has multiple print modes that can be accessed by adjusting the applied electric field strength, nozzle diameter, stand-off distance, and ink properties (viscosity, conductivity, and surface tension). For this work, the cone-jet mode was used to print lines while the multijet mode was used to spray films, as described by Jaworek et al.[51]

All samples were printed on 50 mm (111) or (100) doped silicon wafers held at 190 °C as measured using a T-type thermocouple attached to a thermometer (Omega HH801B). Motion was

https://doi.org/10.1021/acsanm.4c05047
ACS Appl. Nano Mater. XXXX, XXX, XXX−XXX

controlled using a three-axis stage (Newport, XML210-S, XMS50-S, GTS30 V) with a heated bed (Watlow, Ultramic Ceramic Heater). The stage is driven using a Newport XPS Motion Controller. The electrospray bias was generated using a Keysight 33500B Waveform Generator to generate a DC waveform amplified by 1000x using a TREK high voltage amplifier. Custom software is used to control bias and stage movement.[52,53] After centrifuging and immediately before printing, the MOD ink is filtered one last time using a PTFE 0.20 μm filter directly into a 2 mL syringe with a 9.5 mm ID loaded on a syringe pump. The syringe is connected to a 0.06 mm ID (34-gauge) needle using 0.8 mm ID PTFE tubing and Luer lock fittings. During printing, the syringe pump was set to a flow rate of 12 μL/min. Stand-off distances between 3 and 4 mm were used to print lines. From preliminary studies, we found that a stand-off distance of at least 3 mm was required to prevent particle formation at the needle. No clogging was observed when printing at stand-off distances $\geq$3 mm even after printing at 190 °C for several hours.

A bias between 2000 and 2200 V is applied directly to the tip with the bias adjusted to achieve the target print mode. Due to the varying viscosity and conductivity of each ink, the voltage and distance were tuned for each print to achieve a steady, well-focused cone-jet stream to print lines. All lines were 20 mm long and printed at 10 mm/sec with an acceleration of 100 mm/sec^2. Morphology, energy dispersive X-ray spectroscopy, X-ray diffraction, and magnetometry samples were prepared for characterization using the print settings listed above to deposit 200 layer thick lines. Two hundred layers were used to print the lines shown in the Printed Morphology and Composition section because they are consistent with the amount of material per unit area needed to properly characterize the properties of the printed materials using magnetometry and XRD. Additionally, they show density and uniformity across many layers and a large cross section for the iron line. X-ray photoelectron effect spectroscopy, transmission electron microscopy, and Mössbauer effect spectroscopy samples were printed using the print settings listed above; however, the number of layers is discussed in those respective sections.

The printed iron lines discussed in the Resistivity, Mechanical Properties, and Spatial Control sections used a 30 μm micropipette tip rather than the 34-gauge needle and a bias of 1000 to 1350 V. We found that the micropipette tip more consistently produced dense iron lines suitable for resistivity and nanoindentation measurements. The micropipet tip was also used for the spatially controlled composites to improve resolution. The iron film that the cobalt dots were printed on top of in the Spatial Control section was 200 printed layers using a 30 μm micropipet tip, a bias of 3300 V, and a printhead to substrate distance of 7 mm to achieve multijet mode.

Morphology and Composition. Top-down and cross-sectional images showing morphology were obtained using a field emission scanning electron microscope (SEM, Amray 3300 Field Emission) with an accelerating voltage of 20 kV and a working distance of 23 mm. The composition of the alloy was obtained using an attached energy-dispersive X-ray spectroscope (EDS, RaySpec). Cross-sectioned samples shown in the Printed Morphology and Composition section were prepared by scoring the edge of the silicon substrate, breaking the silicon at the scored point, and then directly imaging the cross-section with no mounting or polishing. The cross-sectioned sample shown in the Spatial Control section was mounted in EpoFix and sequentially polished down to 1 μm using diamond suspensions (LECO) for better imaging and EDS mapping.

X-ray Photoelectron Spectroscopy. X-ray photoelectron spectroscopy (XPS) was performed using a Scienta-Omicron HiPP-3 XPS equipped with a R4000 hemispherical analyzer operating in swift acceleration mode and calibrated to the Au 4f region (83.95 eV) of a sputter cleaned Au foil. A focused Al Kα X-ray source (1486.6 eV) was operated with an 800 μm spot size at 300 W. Survey and high-resolution spectra (C 1s, O 1s, N 1s, Fe 2p, Co 2p, Fe 3s, and Co 3s) were acquired at pass energies of 500 and 200 eV, respectively. The analysis chamber pressure was maintained at a level below 5.0×10^{-8} mbar, while the analyzer pressure remained below 1×10^{-9} mbar. The samples were printed on doped silicon and mounted on conductive carbon tape and thus did not require charge neutralization.

Elemental composition for the iron and cobalt samples was quantified by comparing the area of the high-resolution C 1s, O 1s, N 1s, and Fe 2p or Co 2p peaks fit with a Shirley background and further corrected by using a calibrated spectrometer transmission function. The area of the combined Fe 3s and Co 3s regions was used to quantify the total amount of iron and cobalt in the FeCo alloy due to the Co Auger peak overlapping the Fe 2p peak. The Fe 3s and Co 3s region was then fit to determine the ratio of Fe to Co in the alloy, as shown in Figure S2.

An iron film was printed on a (100) silicon wafer by printing 20 mm long parallel lines each consisting of 100 layers; 10 parallel lines were printed by shifting the print head 0.5 mm after each line was printed. The wafer was then diced to obtain a 3 × 3 mm piece of silicon with the iron film on it. The shards for the three samples were then vacuum bagged in the glovebox and transferred to the XPS through an interlock and sample prep box under a nitrogen environment. The samples prepared in a nitrogen glovebox and transferred under nitrogen to the XPS system were never exposed to air.

Mössbauer Effect Spectroscopy. An approximately 11 μm thick iron film was printed on a 100 μm thick (100) silicon wafer (University Wafer 3973) by printing 20 mm long parallel lines each consisting of 100 layers. Thirty parallel lines were printed by shifting the print head 0.5 mm after each line was printed to obtain a film 20 mm × 15 mm × 11 μm ($L \times W \times H$). The day after printing the wafer, the sample was mounted on an 11 mm diameter collimator and loaded into the Mössbauer spectrometer, and spectra were collected. Data were accumulated for 48 h at 296 K using a ^{57}Co−Rh source operating in the triangular constant acceleration mode. A Kr-filled proportional counter and a Wissel data acquisition module (CMCA-550 USB) were used to collect and sort the data into 1024 channels. Velocity calibration and the isomer shift zero value were established with 28.5 μm thick pure bcc (α)-Fe foil. WinNormos V3.0 coupled with the IGOR Pro V6.3 software package was used to fit the magnetic sextet components to the normalized data using a least-squares fitting procedure. The fit variables for each sextet include: internal magnetic hyperfine field, the isomer shift with respect to pure a-iron, and the quadrupole splitting.

Atomic and Crystal Structure. XRD diffractograms were obtained by using a Bruker D2 Phaser diffractometer equipped with a cobalt source. Diffractograms were processed using Diffrac.EVA (Bruker) and HighScore (Malvern Panalytical). Printed line samples were scraped into a powder onto a Bruker single crystal Si low background holder.

Transmission electron microscopy (TEM) samples were prepared by printing a single layer directly onto a 400-mesh copper grid with a carbon film coating (Ted Pella 01844). Thinner edge regions of the printed line were imaged. Transmission electron micrographs and selected area diffraction (SAED) patterns were collected using both an FEI TALOS F200 field emission scanning/transmission electron microscope operated at 200 kV and an FEI Titan 80−300 operated at 300 kV.

Magnetometry. Magnetic hysteresis loops were obtained by using a Quantum Design MPMS3 (SQUID) magnetometer. All DC magnetometry measurements were taken at 300 K with a maximum field of 3 T. Remnant field error was corrected using a palladium standard. Samples were prepared by scraping as printed lines consisting of 200 layers into pure gelatin capsules (size 3) and sandwiched between another half-gel cap. Gel caps were then loaded into clear plastic straws and attached to the sample holder for measurement.

Resistivity. Resistivity measurements were taken on iron lines printed using a 30 μm micropipet tip rather than a 34-gauge needle. This printing method enabled more reproducible lines with similar density to the iron line shown in the Printed Morphology and Composition section. Electrical measurements were collected with a source measurement unit (SMU, Keysight, B2901A) connected to a probe station in a 4-wire Kelvin configuration. The probes were palladium coated and had a tip diameter of 25 μm (Micro-manipulator, 7B-25-HCT). The SMU collected IV data from 0 to

https://doi.org/10.1021/acsanm.4c05047
ACS Appl. Nano Mater. XXXX, XXX, XXX−XXX

10 mA to verify an ohmic IV response. The measured resistance was divided by the inner voltage probe spacing of 0.76 mm to calculate the line resistance and then multiplied by the cross-sectional area of the line measured with a Bruker DektakXT profilometer to obtain the resistivity.

Nanoindentation. Nanoindentation experiments were conducted on a Hysitron Bruker Ti950 equipped with a 10,000 μN maximal load transducer. A Berkovich indenter with a nominal angle of 65.3° was used for testing and was calibrated against a reference fused silica sample. Indentations were evaluated from 250 to 3000 μN peak load with coincident loading/unloading rates of 40 to 400 μN/s to minimize indentation axis drift. Mean hardness and elastic modulus was determined using a peak load of 1750 μN and a load/unload rate of 140 μN/s with a 3 s quasi-static (QS) hold at maximum load, resulting in a QS-trapezoidal testing profile with a 28 s period. The 1750 μN load produced sufficient indentation depth within the calibrated range of the instrument's tip approach function, allowing systematic variations in hardness, retained surface effects from mechanical polishing, and minimized thermal drift for hardness and modulus measurements. Samples were indented under several surface finish conditions (1 μm diamond slurry, 0.05 μm colloidal silica). Three horizontal lines of 20 indents were used to characterize regional variations in nanoindentation hardness and establish statistical accuracy.

RESULTS AND DISCUSSION

Printed Morphology and Composition. The three main inks discussed and characterized in this work are iron, cobalt, and an iron−cobalt mixture that produces an alloy with a nearly 1:1 ratio of Fe:Co (the actual measured ratio was 49:51). The printed composition determined using energy dispersive X-ray spectroscopy (EDS) is shown in Table 1, while the surface composition extracted from X-ray photoelectron spectroscopy (XPS) is shown in Table 2. Quantification of light element residuals in these samples using SEM-EDS is limited due to shadowing effects for any rough surface, reabsorption of low energy X-rays, and inability to detect carbon with our specific EDS.[54] For these reasons, the values given for the oxygen content in Table 1 can be conservatively assumed to represent the lower limit. Based on XPS and Mössbauer (discussed below), much of this oxygen content is believed to be from undecomposed carbonyls.

Table 2. At % Using XPS for Carbon, Oxygen, Nitrogen, Iron, and Cobalt for the Three Printed Samples

printed sample	Fe (at %[a])	Co (at %[a])	C (at %[a])	O (at %[a])	N (at %[a])
Fe	17	–	47	33	3
Co	–	15	61	21	3
FeCo alloy	12	12	50	23	3

[a]10% absolute error and 5% relative error is typical of this XPS.

X-ray photoelectron spectroscopy was used to further explore contamination because, unlike the EDS used in this study, it is sensitive to C and N. High resolution measurements show that there is C, N, and O contamination within the measured region of all three samples. The ratio of iron to cobalt in the printed FeCo alloy is close to 1:1 and agrees with the EDS data. Assuming that all nitrogen contamination comes from the octylamine solvent and that the solvent remains unreacted, we calculate that around 24% of the measured carbon belongs to trapped or adsorbed solvent on the surface of the print (Supporting Information). Additional carbon and oxygen contamination likely comes from incomplete decomposition of the metal carbonyls, which will be discussed in more depth following a discussion of Mössbauer effect spectroscopy.

Mössbauer spectroscopy was performed on the as printed iron sample, and two distinct phases were identified by fitting three components using a least-squares fitting procedure. Figure 2 shows the Mössbauer spectrum; the solid line through the data points is the fitted spectrum, and the stick diagrams identify two broad sextets and a weak but sharp sextet. The weak but sharp sextet represented in green is attributed to a metallic iron phase making up 3% of the area fraction. The two broad sextets (red stick diagrams) are both attributed to an amorphous iron−carbon phase and make up 97% of the area fraction. The identified phases represent a suggested interpretation based on the literature of previous iron pentacarbonyl and amorphous iron carbide studies as well as knowledge of spectral parameters of known Fe-containing phases (pure Fe and Fe-carbides).[30,55−57] The area fractions may serve as an approximation for the iron fractions of the two phases but may need corrections if the Mössbauer recoilless fractions are different for the different phases. The scatter in the baseline in Figure 2 is only 0.04%. The statistical uncertainty in fitting the 3% relative area of the metallic Fe is less than 0.5%, and similarly for the 97% amorphous phase, the relative area uncertainty is less than 0.5%.

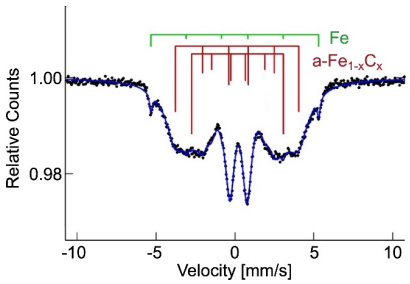

Figure 2. Room-temperature Mössbauer spectrum of the as printed iron ink. The computer fit, represented by the solid blue line, is comprised of a weak but sharp sextet attributed to Fe and two broad sextets attributed to an iron carbon phase. The primary identified phase is an amorphous iron−carbon phase with an area fraction of 97%.

Undecomposed iron carbonyls could explain lack of identified oxide phase in Mössbauer effect spectroscopy but the relatively high (more than 20 at %) oxygen content seen in XPS. An oxide phase would not be visible in Mössbauer effect spectroscopy if the source of oxygen was from carbonyls because the carbon of the carbonyl is directly bonded to the iron while the oxygen is not. Additional evidence for incomplete decomposition is supported by the fact that the printed material is still amorphous and pure amorphous iron would recrystallize at room temperature and atmospheric pressure.[58,59] The incomplete decomposition provides resistance to crystallization because crystallization would require topological changes in the form of Fe−CO bonds breaking and subsequent rearrangement into a topologically ordered network.[60] Terminating carbonyls would also be expected to greatly impact the mechanical properties of the printed material because they would replace stronger iron−iron bonds with electrostatic bonds such as van der Waals forces, which is discussed further in the Mechanical section.

https://doi.org/10.1021/acsanm.4c05047
ACS Appl. Nano Mater. XXXX, XXX, XXX−XXX

Printed morphology varies greatly between different ink compositions and has minor differences observed between prints for the same ink. As shown in Figure 3, printed iron has

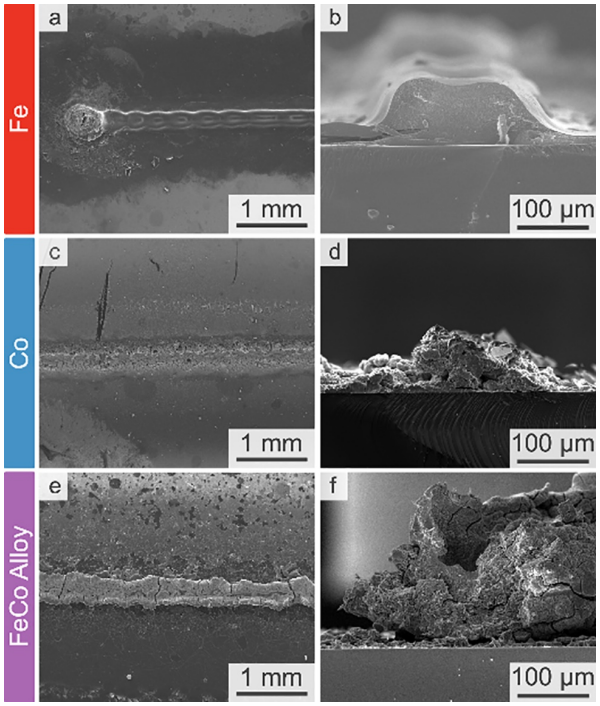

Figure 3. (a, c, and e) Top-down SEM micrographs of 200 layers for iron, cobalt, and the FeCo alloy, respectively. (b, d, and f) Cross section of 200 layers for iron, cobalt, and the FeCo alloy, respectively. Dense lines with minimal cracking have been achieved with Fe inks. Co inks produce the most porous prints as assessed through image analysis.

the least cracking and highest density (Figures 3a and 3b) while printed cobalt is the most porous with significant cracking (Figures 3c and 3d). The FeCo alloy also exhibits cracking and porosity; however, it is visually less than that of the monometallic cobalt sample. There are several possibilities for the difference in print morphology. One possibility is the difference in the decomposition temperatures of organometallic precursors in relation to the boiling point of octylamine. Octylamine boils at 176 °C, which is closer to the decomposition temperature range of triiron dodecacarbonyl (110 to 170 °C) as determined using thermogravimetric analyis,[29] whereas dicobalt octacarbonyl decomposes earlier at temperatures ranging from 108 to 162 °C as determined using differential scanning calorimetry.[61] Studies of reactive silver inks have shown that using solvents with higher boiling points can increase the porosity of the resulting silver by allowing particles to form within the droplet while the solvent is slowly evaporating.[2,62] Nanoparticle formation in the printed ink before solvent evaporation could also lead to cracking due to capillary drying stresses.[63,64] It is possible that the Co reactive ink is showing similar behavior, with more Co particles forming in the octylamine before the octylamine boils off. Another potential explanation for porosity and cracking is the dynamic rheology of the ink coupled with the decomposition mechanisms, where the ink thickens as particles precipitate, which could trap the carbon monoxide reaction products and vaporized solvent, leading to a porous film. As observed in Figure 3f and Figure S3, printed lines are sometimes thicker on the sides than in the middle. This may be attributed to the coffee ring effect, where capillary flow brings particles to the edges of the line. However, the steep sidewalls observed in the FeCo alloy (Figures 3e and 3f) suggest other phenomena might be dominating, such as an autofocusing effect observed during electrohydrodynamic (EHD) printing.[65] This autofocusing effect may also be responsible for the trapezoidal cross section of the printed iron line shown in Figure 3b. Another explanation could be the incoming stream of ink cutting a channel into a porous/broken film. The actual cause of this phenomenon is under investigation. As observed in Figure 3a, most of the printed material builds upon a 300 to 500 μm thick line; however, spray ends up on either side of the line, forming a thin film of metal 1 to 3 mm wide. While this background film/overspray can even be observed in other works that use EHD printing to deposit reactive inks with very high resolution and aspect ratios,[47,66] the large-scale background contamination seen in this work is attributed to the 3 mm minimum stand-off distance required to prevent particle formation at the print head. Resolution could be improved by cooling the print head to print at much closer stand-off distances without clogging the nozzle.[24] Future optimization of cobalt inks by evaluating the relationship between the solvent boiling point and metal carbonyl decomposition temperature or further tuning of EHD printing parameters may allow for dense prints to be printed regardless of the alloy composition. Overall, EHD printing of metal carbonyl MOD inks has room for improved density and resolution, but it already shows promise for producing continuous amorphous and magnetic metals through a scalable process.

Deposition of continuous amorphous iron on a temperature sensitive substrate is demonstrated by printing an iron line and film across polyimide Kapton tape stuck to a silicon wafer, as shown in Figure S11. The same conditions used to print the iron line shown in Figures 3a and 3b were used to print the 50 layer thick iron line across the Kapton tape. The iron film was deposited by printing 20 layers with an increased stand-off distance of 7 mm and voltage of 5000 V. Although the nonconductive Kapton tape causes increased surface roughness, cracking, overspray, line width, and varied morphology compared to Figures 3a and 3b, the Kapton tape was successfully metallized with amorphous iron and no damage to the tape was observed.

Atomic Structure. XRD and TEM determined that iron and iron−cobalt alloys are amorphous, while cobalt is nanocrystalline in an amorphous matrix. The XRD diffractograms for the three as printed samples (Figure 4) do not show any well-defined peaks, but rather one broad hump around a 2θ 50°, which is indicative of amorphous or nanocrystalline material. The as printed cobalt sample has a slightly more defined and sharper peak inside a broad hump of around 51.5°.

The as printed iron, cobalt, and iron−cobalt alloy were then encapsulated in quartz tubes flushed with argon and annealed at 700 °C for 10 min to examine their recrystallization behavior. XRD diffractograms for the crystallized samples in Figure 4 show the iron sample (HT Fe) crystallized at this temperature produces iron carbide. Shpaisman et al. heated triiron dodecacarbonyl in an argon flow over a range of temperatures including 600 °C, which has a diffractogram very similar to that of the heat-treated iron in this work.[29] The cobalt (HT Co) and iron−cobalt alloy (HT FeCo alloy)

https://doi.org/10.1021/acsanm.4c05047
ACS Appl. Nano Mater. XXXX, XXX, XXX−XXX

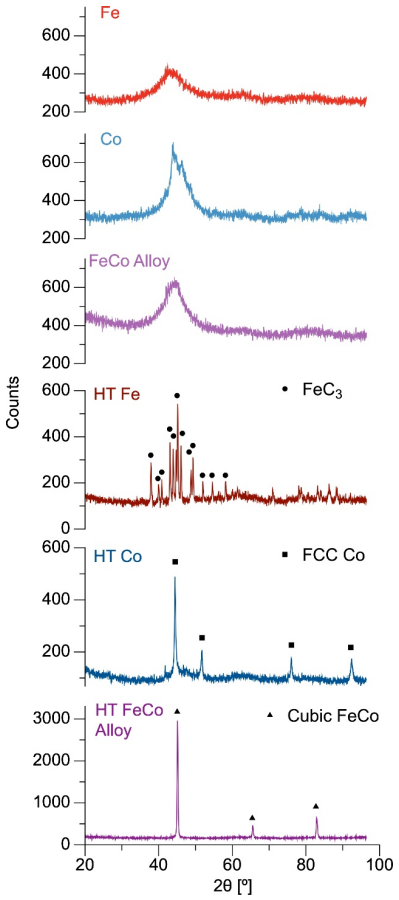

Figure 4. Diffraction pattern for the as printed Fe and Co and the FeCo alloy and all three samples after being heat treated (HT) at 700 °C for 10 min. The three printed patterns show a broad bump around 50°. The cobalt sample has a sharper peak inside the broad hump at around 51.5°. After heat treatment, the Fe ink crystallizes to FeC_3, while the Co and FeCo inks produce metallic material with no visible oxide or carbide peaks.

produce metallic cobalt and a metallic iron−cobalt alloy, respectively. The heat-treated Co diffractogram has visible peaks at (111), (200), (220), and (311), all corresponding to the face centered cubic phase of Co. The FeCo alloy diffractogram shows a clear diffraction pattern, with (110), (200), and (220) peaks corresponding to the cubic phase of FeCo. No oxide or carbide peaks are visible for the crystallized Co or FeCo alloy.

To fully determine if the as printed samples were amorphous or nanocrystalline, high resolution TEM (HR-TEM) and selected area diffraction (SAED) were utilized. The HR-TEM and SAED of the printed iron (Figures 5a−5c) and the FeCo alloy (Figures 5g−5i) samples show almost completely amorphous material. HR-TEM images for both printed iron and the FeCo alloy samples appear to have the same fine-scale morphology, lacking evident crystalline domains and exhibiting microstructural homogeneity. Both SAED patterns are comprised of diffuse rings and lack sharp diffraction spots. As seen in Figures 5d−5f, printed cobalt is significantly more crystalline. The HR-TEM images displayed in Figure 5e show many grains embedded in an amorphous matrix. To determine the average size of these nanocrystals, only the darker oblong nanocrystals were measured because they had a greater contrast than the surrounding area and were clearly discrete. The average length and width were 6.6 and 3.0 nm, respectively. Figure S6 provides an image of the measured region as well as a histogram of the measured crystallites. SAED of the printed cobalt sample (Figure 5f) reveals a combination of bright, sharp rings and diffuse ones. It also shows individual spots that represent specific grain orientations; however, a preferred orientation and crystallographic texture are not identified. The ability to make amorphous or nanocrystalline metal using the same print conditions, by simply changing the ink, is beneficial when varying printed composition, as discussed in the spatial control section.

Magnetic Response. Fe, Co, and FeCo alloys are ferromagnetic and commonly used as soft magnets.[12,67] DC hysteresis loops, as shown in Figure 6, were used to determine the magnetic saturation, coercivity, and remanence. Figure S7 shows the full 3 to −3 T sweep for the three curves shown in Figure 6 on separate plots and with error bars. Hysteresis loops were collected by sweeping from 3 to −3 T at 300 K. The FeCo alloy in this work had the highest magnetic saturation (M_s), while monometallic Co had the lowest M_s, although all three samples had similar enough values to fall within the margin of error shown in Table 3. Magnetic saturation for the as printed iron had similar saturation to what was previously found for iron nanoparticles synthesized from thermal decomposition of triiron dodecacarbonyl (89 vs 94 emu/g) and higher coercivity (90 Oe vs. 57 Oe).[29] The Fe, Co, and FeCo alloy printed using the reactive inks in this work had higher magnetic saturation and lower coercivity than nickel printed from a reactive ink, which had an M_s of 30 emu/g and coercivity 120 Oe.[7] The difference between the M_s, coercivity, and remanence of the as printed materials compared to their respective crystalline counterparts is attributed to the high degree of contamination and the amorphous atomic structure stabilized by this contamination. Although these printed metals have higher coercivity than what is used for amorphous soft magnets, they could have applications as semihard FeCo-based magnets.[12,68] Magnetic saturation, coercivity, and remanence increased for all three samples after they were heat treated at 700 °C, as shown in Table S2 and Figure S8. Since magnetic saturation and coercivity are intrinsic properties, a single printed layer of these materials may be an effective magnetically active layer depending on the application. Future work will explore tuning the coercivity by adjusting remanent contamination levels.

Electrical and Mechanical Properties of Printed Iron. Only the printed iron's electrical and mechanical properties were measured due to the cracked and porous nature of the printed cobalt containing inks. The printed iron exhibited metallic behavior, evidenced by ohmic IV characteristics (Figure S9) with an electrical resistivity of 6 $\mu\Omega$·m, approximately 63 times that of bulk iron. This deviation is primarily attributed to the high remnant carbon, oxygen, and speculated undecomposed carbonyl contamination. The remnant contamination is believed to stabilize the amorphous structure of the printed iron and increase resistivity. Remnant carbonyls would further increase resistivity because they would replace iron−iron bonds with terminating carbonyl bonds.

Nanoindentation was performed on the cross-section of the as printed iron line to determine the mechanical hardness and elastic modulus. The iron line had a mean hardness (H) of 3.9 ± 0.4 GPa and reduced elastic modulus (E_r) of 62 ± 6 GPa. Although the nanoindentation hardness is relatively low for an

https://doi.org/10.1021/acsanm.4c05047
ACS Appl. Nano Mater. XXXX, XXX, XXX−XXX

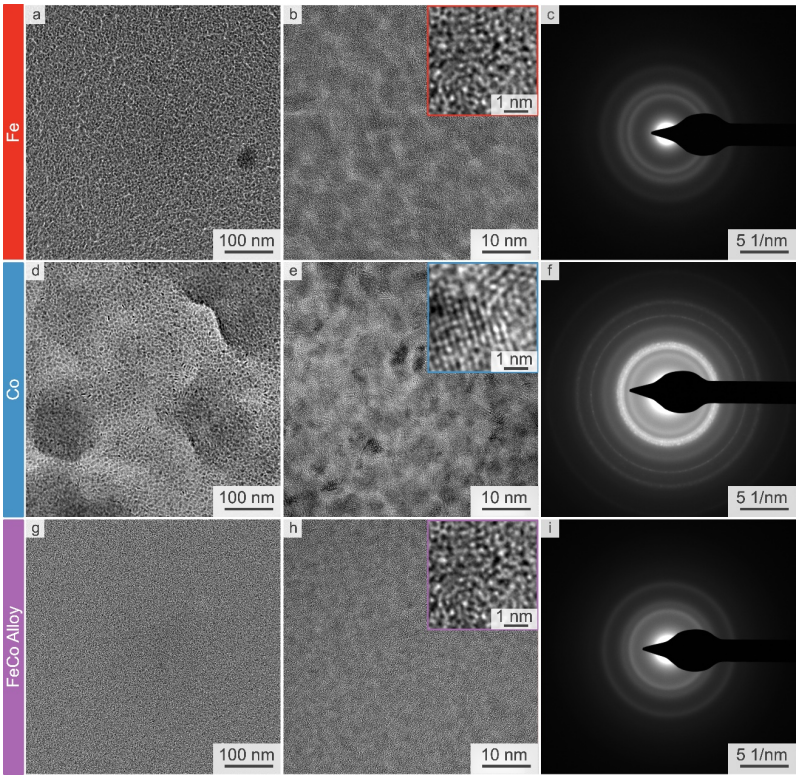

Figure 5. (a, d, and g) TEM micrographs of mostly amorphous iron, nanocrystalline cobalt, and mostly amorphous FeCo alloy, respectively. The FeCo alloy is the most uniform followed by iron, while cobalt is the least visually uniform. (b, e, and h) HR-TEM micrographs of iron, cobalt, and the FeCo alloy. (c, f, and i) SAED of iron, cobalt, and the FeCo Alloy. SAED images of both Fe and the FeCo alloy have diffuse broad rings indicative of an amorphous structure, while the cobalt sample has sharper brighter rings as well as individual bright spots indicative of many nanocrystalline grains.

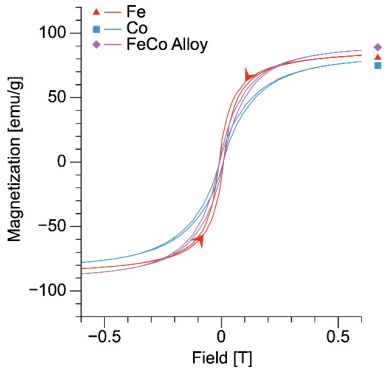

Figure 6. DC hysteresis loops collected at T = 300 K for the iron, cobalt, and iron−cobalt alloy. All three samples have very similar magnetization and coercivity.

Table 3. Magnetic Saturation, Coercivity, and Remanence for As Printed Fe, Co, and FeCo Alloy

name	saturation (emu/g)	coercivity (Oe)	remanence (emu/g)
Fe	89.3 ± 4.4	89.7 ± 0.1	13.3 ± 0.6
Co	85.3 ± 4.2	73.2 ± 1.0	5.4 ± 0.3
FeCo alloy	93.8 ± 4.6	76.1 ± 1.0	7.8 ± 0.4

amorphous metal, it is very similar to that of annealed pure iron.[49] The low hardness is attributed to carbonyl contamination. This contamination would effectively replace Fe−Fe bonds with van der Waals forces, lowering the bonding strengths while increasing the degrees-of-freedom for greater plasticity. Therefore, hardness would be expected to increase with decreasing contamination until the contamination no longer stabilizes the amorphous matrix, and the as printed material is crystalline. Future work will be focused on decreasing this contamination and determining how it affects material properties.

Nanoindentation was performed using a range of ultimate loads (250 to 3000 μN) and constant load/unload periods generating strain rates of 40 to 400 μN/s. As peak load was increased (increasing indentation depth), Figure 7 shows a drop in respective values for hardness and elastic modulus. Nix et al. attributed this to size effects characteristic with indentation correlating with an increase in the material's regional pile-up ratio,[69] while others such as Ramamurty et al. suggest such size effects are unlikely to be responsible for statistically significant changes in hardness with increasing load due to the lack of a material length scale in amorphous metal alloys.[70]

Spatial Control. Additive manufacturing processes are well suited to create composites and can reduce the number of processing steps necessary to pattern or layer materials when compared with traditional fabrication methods such as photolithography and evaporation/sputtering. To demonstrate this ability, iron and cobalt inks were printed as layers and patterned dots to show vertical and lateral control, respectively. Since the as printed iron ink produces amorphous iron while the as printed cobalt ink produces nanocrystalline cobalt,

https://doi.org/10.1021/acsanm.4c05047
ACS Appl. Nano Mater. XXXX, XXX, XXX−XXX

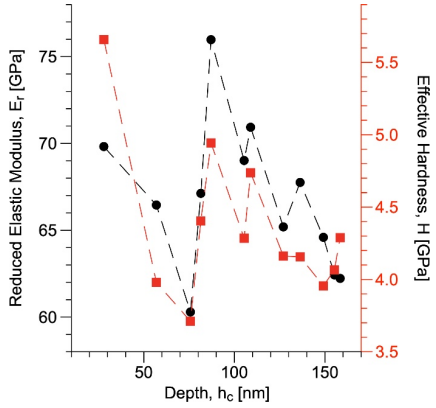

Figure 7. Reduced elastic modulus and nanoindentation hardness (GPa) vs indentation depth.

controlling both the elemental composition and the correlated atomic structure is enabled by simply printing each ink in different locations.

Figures 8a–8d show SEM micrographs and EDS maps of graded iron and cobalt layers printed on top of each other with

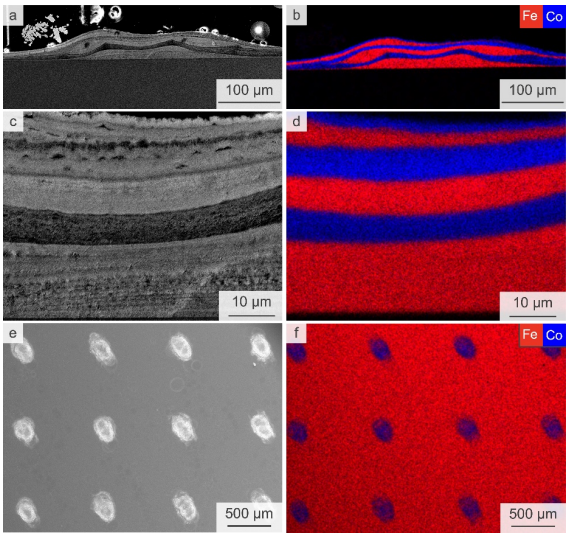

Figure 8. (a and c) Cross-section SEM micrographs. (b and d) EDS map of alternating stacked layers of iron (red) and cobalt (blue) shows an ability to control composition vertically. (e) Top-down SEM micrograph of cobalt dots on a uniform printed iron film. (f) EDS map of cobalt (blue) dots printed on an iron (red) film shows an ability to control composition laterally.

the thickest layers closest to the substrate and decreasing in thickness moving away from it. Four hundred layers of iron were printed first with 200 layers of cobalt on top. Next, 200 layers of iron were printed, followed by 100 layers of cobalt. Finally, 100 layers of iron and 50 layers of cobalt were printed on top. The grading is not perfect due to needle alignment limitations with our current setup with subsequent layers not lining up perfectly with layers below it, as seen in Figures 8a and 8b. This is most visible with the top iron layer, where it appears as if the top iron layer is shifted left by more than 100 μm. Figures 8e and 8f show cobalt dots on top of an iron film. The uniform iron film was printed by spraying 200 layers of iron followed by 10 layers of cobalt dots in a 5 × 5 grid pattern with 1 mm spacing. A higher magnification micrograph of the uniform film printed using the iron ink is shown in Figure S10. Figures 8a–8d show vertical resolution on the tens of micrometers, while Figures 8e and 8f show the lateral resolution is on the millimeter scale. This process demonstrates the ability to arbitrarily control the thickness and position of both elemental composition and atomic structure, providing new ways to spatially pattern amorphous and crystalline material and produce devices with graded, layered, and functional architectures. The spatial control shown in this work could hypothetically be used to print an inductor using silver and iron reactive inks or layered amorphous and crystalline shock absorbing materials discussed in the introduction.

CONCLUSION

This work introduces particle-free iron, cobalt, and iron–cobalt MOD inks with the goal of developing reactive inks to print materials for magnetic or structural applications. TEM images and SAED along with XRD determined that printed triiron dodecacarbonyl inks produced fully amorphous Fe, dicobalt octacarbonyl inks produced nanocrystalline cobalt in an amorphous matrix, and a mixture of the two produced amorphous iron–cobalt alloys. SEM revealed that the morphology of the printed iron reactive ink is dense and uniform, whereas the inks with cobalt produce more porous material. High-temperature heat treatments on the as printed metals showed that the amorphous or nanocrystalline metal can be recrystallized with the printed iron recrystallizing to iron carbide and the printed Co and FeCo alloy recrystallizing to metallic Co and FeCo, respectively. EDS, XPS, and Mössbauer indicate some remanent carbonyls remain in the film from incomplete decomposition for all three printed inks. This contamination is believed to significantly affect the material properties of the as printed material while stabilizing the amorphous structure. We speculate that some iron–iron bonds are replaced with terminating carbonyls, which lower the elastic modulus and nanoindentation hardness of the amorphous printed iron compared to other amorphous metals. Magnetic saturation, coercivity, and remanence were measured at 300 K using a SQUID magnetometer to show that the printed iron ink had magnetic properties similar to those of other chemically synthesized amorphous iron. Metallization of temperature sensitive substrates was demonstrated by metallizing polyimide Kapton tape with continuous amorphous iron. Fe and Co reactive inks were patterned in 2.5D to demonstrate spatial control over composition and crystallinity. In summary, this work designed, printed, and characterized novel particle-free iron and cobalt reactive inks which can deposit continuous, amorphous, and magnetic metal and can be combinatorially printed to produce metallic composites or alloys.

ASSOCIATED CONTENT

Supporting Information

The Supporting Information is available free of charge at https://pubs.acs.org/doi/10.1021/acsanm.4c05047.

Additional data and figures showing additional ink compositions, the XPS fit used to estimate composition, a histogram of the cobalt nanoparticle sizes, additional magnetic data, the ohmic response of the as printed iron

https://doi.org/10.1021/acsanm.4c05047
ACS Appl. Nano Mater. XXXX, XXX, XXX–XXX

line, and additional SEM micrographs of the printed iron film and a single layer of printed iron (PDF)

AUTHOR INFORMATION

Corresponding Author

Owen J. Hildreth − *Department of Mechanical Engineering, Colorado School of Mines, Golden, Colorado 80401, United States;* orcid.org/0000-0001-5358-9080; Email: ohildreth@mines.edu

Authors

Collin E. Miller − *Materials Science Department, Colorado School of Mines, Golden, Colorado 80401, United States;* orcid.org/0000-0002-0573-3858

Joshua Edwards − *Department of Metallurgical and Materials Engineering, Colorado School of Mines, Golden, Colorado 80401, United States*

Chris Matsumura − *Department of Physics, University of Washington, Seattle, Washington 98195, United States*

Matthew Michael Schneider − *Materials Science and Technology Division, Los Alamos National Laboratory, Los Alamos, New Mexico 87544, United States;* orcid.org/0000-0002-7425-7736

Serena Eley − *Department of Electrical and Computer Engineering, University of Washington, Seattle, Washington 98195, United States; Department of Physics, Colorado School of Mines, Golden, Colorado 80401, United States;* orcid.org/0000-0002-2928-5316

Suveen N. Mathaudhu − *Department of Metallurgical and Materials Engineering, Colorado School of Mines, Golden, Colorado 80401, United States*

Complete contact information is available at: https://pubs.acs.org/10.1021/acsanm.4c05047

Notes

The authors declare no competing financial interest.

ACKNOWLEDGMENTS

We acknowledge Professors Don Williamson and Kenneth Steirer, in the Department of Physics at the Colorado School of Mines, for assistance with Mössbauer spectroscopy and XPS, respectively. O.J.H. and C.E.M. gratefully acknowledge the support from the National Science Foundation (CAREER 1944516). Contributions from S.E. and C.M. at the University of Washington were supported by NSF DMR 2325089. J.E. was supported by the U.S. Department of Education under a Graduate Assistance in Areas of National Need (GAANN) Fellowship (Grant P200A210134). This work was performed, in part, at the Center for Integrated Nanotechnologies, an Office of Science User Facility operated for the U.S. Department of Energy (DOE) Office of Science. Los Alamos National Laboratory, an affirmative action equal opportunity employer, is managed by Triad National Security, LLC for the U.S. Department of Energy's NNSA, under Contract 89233218CNA000001.

REFERENCES

(1) Mamidanna, A.; Lefky, C.; Hildreth, O. Drop-on-Demand Printed Microfluidics Device with Sensing Electrodes Using Silver and PDMS Reactive Inks. *Microfluid. Nanofluidics* **2017**, *21* (11), 172.

(2) DiGregorio, S. J.; Martinez-Szewczyk, M.; Raikar, S.; Bertoni, M. I.; Hildreth, O. J. Investigation of Reactive Silver Ink Formula for Reduced Silver Consumption in Silicon Heterojunction Metallization. *ACS Appl. Energy Mater.* **2023**, *6* (5), 2747−2757.

(3) Xu, H.; Tang, X.; Sun, H.; Zhao, H.; Li, M. Conductivity of Silver and Copper Film Printed by Particle-Free Reactive Inks. *2017 18th Int. Conf. Electron. Packag. Technol. (ICEPT)* **2017**, 1470−1473.

(4) Zhou, Y.; Xu, Z.; Bai, H.; Knapp, C. E. Room Temperature Electronic Functionalization of Thermally Sensitive Substrates by Inkjet Printing of a Reactive Silver-Based MOD Ink. *Adv. Mater. Technol.* **2023**, *8* (8), No. 2201557. (1−11)

(5) DiGregorio, S. J.; Hildreth, O. J. Particle-Less Reactive Inks. In *Smart Multifunctional Nano-Inks Fundamentals and Emerging Applications*; Elsevier, 2023; pp 125−158. DOI: 10.1016/b978-0-323-91145-0.00011-6.

(6) Yang, W.; List-Kratochvil, E. J. W.; Wang, C. Metal Particle-Free Inks for Printed Flexible Electronics. *J. Mater. Chem. C* **2019**, *7* (48), 15098−15117.

(7) Mahajan, C. G.; Alfadhel, A.; Irving, M.; Kahn, B. E.; Borkholder, D. A.; Williams, S. A.; Cormier, D. Magnetic Field Patterning of Nickel Nanowire Film Realized by Printed Precursor Inks. *Materials* **2019**, *12* (6), 928.

(8) Wu, L.; Dong, Z.; Li, F.; Zhou, H.; Song, Y. Emerging Progress of Inkjet Technology in Printing Optical Materials. *Adv. Opt. Mater.* **2016**, *4* (12), 1915−1932.

(9) An, B. W.; Kim, K.; Lee, H.; Kim, S.; Shim, Y.; Lee, D.; Song, J. Y.; Park, J. High-Resolution Printing of 3D Structures Using an Electrohydrodynamic Inkjet with Multiple Functional Inks. *Adv. Mater.* **2015**, *27* (29), 4322−4328.

(10) Jiraskova, Y.; Zazimal, F.; Bursik, J.; Svoboda, T.; Dzik, P.; Homola, T. Structural and Physical Characterization of Iron-Oxide Based Inks for Inkjet Printing. *J. Magn. Magn. Mater.* **2022**, *562*, No. 169810.

(11) Popova, A. N. Synthesis and Characterization of Iron-Cobalt Nanoparticles. *J. Phys. Conf Ser.* **2012**, *345* (1), No. 012030.

(12) Silveyra, J. M.; Ferrara, E.; Huber, D. L.; Monson, T. C. Soft Magnetic Materials for a Sustainable and Electrified World. *Science* **2018**, *362* (6413), n/a.

(13) Shirsath, S. E.; Wang, D.; Zhang, J.; Morisako, A.; Li, S.; Liu, X. Single-Crystal-like Textured Growth of CoFe2O4 Thin Film on an Amorphous Substrate: A Self-Bilayer Approach. *ACS Appl. Electron. Mater.* **2020**, *2* (11), 3650−3657.

(14) Vaseem, M.; Ghaffar, F. A.; Farooqui, M. F.; Shamim, A. Iron Oxide Nanoparticle-Based Magnetic Ink Development for Fully Printed Tunable Radio-Frequency Devices. *Adv. Mater. Technol.* **2018**, *3* (4), No. 1700242. (1−11)

(15) Sundaram, S.; Skouras, M.; Kim, D. S.; van den Heuvel, L.; Matusik, W. Topology Optimization and 3D Printing of Multimaterial Magnetic Actuators and Displays. *Sci. Adv.* **2019**, *5* (7), No. eaaw1160.

(16) Yoo, H. J. *Reactive Binders for Metal Parts Produced By Three Dimensional Printing*; Massachusetts Institute of Technology, 1997.

(17) Walker, S. B.; Lewis, J. A. Reactive Silver Inks for Patterning High-Conductivity Features at Mild Temperatures. *J. Am. Chem. Soc.* **2012**, *134* (3), 1419−1421.

(18) Valeton, J. J. P.; Hermans, K.; Bastiaansen, C. W. M.; Broer, D. J.; Perelaer, J.; Schubert, U. S.; Crawford, G. P.; Smith, P. J. Room Temperature Preparation of Conductive Silver Features Using Spin-Coating and Inkjet Printing. *J. Mater. Chem.* **2010**, *20* (3), 543−546.

(19) Reiser, A.; Lindén, M.; Rohner, P.; Marchand, A.; Galinski, H.; Sologubenko, A. S.; Wheeler, J. M.; Zenobi, R.; Poulikakos, D.; Spolenak, R. Multi-Metal Electrohydrodynamic Redox 3D Printing at the Submicron Scale. *Nat. Commun.* **2019**, *10* (1), 1853.

(20) Knapp, C. E.; Chemin, J.; Douglas, S. P.; Ondo, D. A.; Guillot, J.; Choquet, P.; Boscher, N. D. Room-Temperature Plasma-Assisted Inkjet Printing of Highly Conductive Silver on Paper. *Adv. Mater. Technol.* **2018**, *3* (3), No. 1700326.

(21) Park, J.-H.; Lee, J.-W.; Ma, Y.-W.; Kang, B.-S.; Hong, S.-M.; Shin, B.-S. Direct Laser Interference Ink Printing Using Copper Metal−Organic Decomposition Ink for Nanofabrication. *Nanomaterials* **2022**, *12* (3), 387.

(22) Mamidanna, A.; Song, Z.; Lv, C.; Lefky, C. S.; Jiang, H.; Hildreth, O. J. Printing Stretchable Spiral Interconnects Using Reactive Ink Chemistries. *ACS Appl. Mater. Interfaces* **2016**, *8* (20), 12594−12598.
(23) Zeng, M.; Du, Y.; Jiang, Q.; Kempf, N.; Wei, C.; Bimrose, M. V.; Tanvir, A. N. M.; Xu, H.; Chen, J.; Kirsch, D. J.; Martin, J.; Wyatt, B. C.; Hayashi, T.; Saeidi-Javash, M.; Sakaue, H.; Anasori, B.; Jin, L.; McMurtrey, M. D.; Zhang, Y. High-Throughput Printing of Combinatorial Materials from Aerosols. *Nature* **2023**, *617* (7960), 292−298.
(24) Lefky, C. S.; Mamidanna, A.; Hildreth, O. J. Ultra Near-Field Electrohydrodynamic Cone-Jet Breakup of Self-Reducing Silver Inks. *J. Electrost.* **2018**, *96*, 85−89.
(25) Zhang, B.; He, J.; Li, X.; Xu, F.; Li, D. Micro/Nanoscale Electrohydrodynamic Printing: From 2D to 3D. *Nanoscale* **2016**, *8* (34), 15376−15388.
(26) Mkhize, N.; Bhaskaran, H. Electrohydrodynamic Jet Printing: Introductory Concepts and Considerations. *Small Sci.* **2022**, *2* (2), No. 2100073.
(27) Bloemacher, D. Carbonyl Iron Powders: Its Production and New Developments. *Met. Powder Rep.* **1990**, *45* (2), 117−119.
(28) Watt, J.; Bleier, G. C.; Austin, M. J.; Ivanov, S. A.; Huber, D. L. Non-Volatile Iron Carbonyls as Versatile Precursors for the Synthesis of Iron-Containing Nanoparticles. *Nanoscale* **2017**, *9* (20), 6632−6637.
(29) Shpaisman, N.; Bauminger, E. R.; Margel, S. One-Step Synthesis of Air-Stable Nanocrystalline Iron Particles by Thermal Decomposition of Triiron Dodecacarbonyl. *J. Alloy. Compd.* **2008**, *454* (1−2), 89−96.
(30) van Wonterghem, J.; Mørup, S.; Charles, S. W.; Wells, S.; Villadsen, J. Formation of a Metallic Glass by Thermal Decomposition of Fe(CO)5. *Phys. Rev. Lett.* **1985**, *55* (4), 410−413.
(31) Cheng, I.; Kelly, J. P.; Novitskaya, E.; Eliasson, V.; Hodge, A. M.; Graeve, O. A. Mechanical Properties of an Fe-Based SAM2 × 5−630 Metallic Glass Matrix Composite with Tungsten Particle Additions. *Adv. Eng. Mater.* **2018**, *20* (9), No. 1800023.
(32) Souza, C. A. C.; Ribeiro, D. V.; Kiminami, C. S. Corrosion Resistance of Fe-Cr-Based Amorphous Alloys: An Overview. *J. Non-Cryst. Solids* **2016**, *442*, 56−66.
(33) Zhang, P.; Tan, J.; Tian, Y.; Yan, H.; Yu, Z. Research Progress on Selective Laser Melting (SLM) of Bulk Metallic Glasses (BMGs): A Review. *Int. J. Adv. Manuf. Technol.* **2022**, *118* (7−8), 2017−2057.
(34) Cuan, X.; Lin, Y.; Liu, Z.; Zhang, B.; Li, N.; Pan, J. On the Impact Toughness of Amorphous/Crystalline Metallic Laminates. *J. Mater. Res. Technol.* **2023**, *26*, 3756−3767.
(35) Greer, A. L. Metallic Glasses. *Science* **1995**, *267*, 1947−1953.
(36) Inoue, A.; Kato, A.; Zhang, T.; Kim, S. G.; Masumoto, T. Mg−Cu−Y Amorphous Alloys with High Mechanical Strengths Produced by a Metallic Mold Casting Method. *Mater. Transactions Jim* **1991**, *32* (7), 609−616.
(37) DAVIES, H. A.; AUCOTE, J.; HULL, J. B. Amorphous Nickel Produced by Splat Quenching. *Nat. Phys. Sci.* **1973**, *246* (149), 13−14.
(38) Ozden, M. G.; Morley, N. A. Laser Additive Manufacturing of Fe-Based Magnetic Amorphous Alloys. *Magnetochemistry* **2021**, *7* (2), 20.
(39) Schultz, L. Formation of Amorphous Metals by Mechanical Alloying. *Mater. Sci. Eng.* **1988**, *97*, 15−23.
(40) Hubler, G. K.; Singer, I. L.; Clayton, C. R. Mechanical and Chemical Properties of Tantalum-Implanted Steels. *Mater. Sci. Eng.* **1985**, *69* (1), 203−210.
(41) Nomura, K.; Tanaka, J.; Ujihira, Y.; Takahashi, T.; Uchida, Y. Mössbauer and EXAFS Studies of Amorphous Iron Produced by Thermal Decomposition of Carbonyl Iron in Liquid Phase. *Hyperfine Interact.* **1990**, *56* (1−4), 1711−1716.
(42) Linderoth, S./r.; Mo/rup, S. Amorphous TM1− x B x Alloy Particles Prepared by Chemical Reduction (Invited). *J. Appl. Phys.* **1991**, *69* (8), 5256−5261.
(43) Lauriat, J.-P. Study by X-Ray and Neutron Diffraction of the Structure of Ex-Carbonyl Amorphous Iron. *J. Non-Cryst. Solids* **1983**, *55* (1), 77−91.
(44) Suslick, K. S.; Choe, S.-B.; Cichowlas, A. A.; Grinstaff, M. W. Sonochemical Synthesis of Amorphous Iron. *Nature* **1991**, *353* (6343), 414−416.
(45) Li, Q.; Wang, G.; Song, X.; Fan, L.; Hu, W.; Xiao, F.; Yang, Q.; Ma, M.; Zhang, J.; Liu, R. Ti50Cu23Ni20Sn7 Bulk Metallic Glasses Prepared by Mechanical Alloying and Spark-Plasma Sintering. *J. Mater. Process. Technol.* **2009**, *209* (7), 3285−3288.
(46) Cardinal, S.; Pelletier, J. M.; Qiao, J. C.; Bonnefont, G.; Xie, G. Influence of Spark Plasma Sintering Parameters on the Mechanical Properties of Cu50Zr45Al5 Bulk Metallic Glass Obtained Using Metallic Glass Powder. *Mater. Sci. Eng.: A* **2016**, *677*, 116−124.
(47) Porenta, N.; Nydegger, M.; Menétrey, M.; Hammadi, S.; Reiser, A.; Spolenak, R. Micron-Scale Additive Manufacturing of Binary and Ternary Alloys by Electrohydrodynamic Redox 3D Printing. *Mater. Des.* **2023**, *234*, No. 112364.
(48) Mohebi, M. M.; Evans, J. R. G. A Drop-on-Demand Ink-Jet Printer for Combinatorial Libraries and Functionally Graded Ceramics. *J. Comb. Chem.* **2002**, *4* (4), 267−274.
(49) Kong, J.; Du, D.; Song, A.; Zhang, F.; Huang, W. Surface Physical and Chemical Modification of Pure Iron by Using Atmospheric Pressure Plasma Treatment. *Materials* **2020**, *13* (21), 4775.
(50) Zhang, C.; Zhou, H.; Liu, L. Laminar Fe-Based Amorphous Composite Coatings with Enhanced Bonding Strength and Impact Resistance. *Acta Mater.* **2014**, *72*, 239−251.
(51) Jaworek, A.; Krupa, A. CLASSIFICATION OF THE MODES OF EHD SPRAYING. *J. Aerosol Sci.* **1999**, *30* (7), 873−893.
(52) Barnes, C.; Henke, L.; Henke, L.; Krukov, I.; Hildreth, O. SwiftVISA: Controlling Instrumentation with a Swift-Based Implementation of the VISA Communication Protocol. *J. Open Source Softw.* **2023**, *8* (83), 4752.
(53) Barnes, C.; Hildreth, O. https://github.com/HildrethResearchGroup/Fifi (accessed 2020-08-01).
(54) Newbury, D. E.; Ritchie, N. W. M. Faults and Foibles of Quantitative Scanning Electron Microscopy/Energy Dispersive x-Ray Spectrometry (SEM/EDS). *Scanning Microsc. 2012: Adv. Microsc. Technol. Déf., Homel. Secur., Forensic, Life, Environ., Ind. Sci.* **2012**, 837803−837812.
(55) Van Wonterghem, J.; Mørup, S.; Charles, S. W; Wells, S. An Investigation of the Chemical Reactions Leading to the Formation of Ultrafine Amorphous Fe100−xcx Alloy Particles. *J. Colloid Interface Sci.* **1988**, *121* (2), 558−563.
(56) Long, G. J.; Hautot, D.; Pankhurst, Q. A.; Vandormael, D.; Grandjean, F.; Gaspard, J. P.; Briois, V.; Hyeon, T.; Suslick, K. S. Mössbauer-Effect and x-Ray-Absorption Spectral Study of Sonochemically Prepared Amorphous Iron. *Phys. Rev. B* **1998**, *57* (17), 10716−10722.
(57) Bauer-Grosse, E.; Le Caer, G. Structural Changes of Amorphous Fe1−xCx Alloys at x & 0.32. *Mater. Sci. Eng.* **1988**, *99* (1−2), 31−33.
(58) Bhadeshia, H. K. D. H. Review: Pure, Amorphous Iron. *J. Mater. Sci.* **2024**, *59* (25), 11278−11287.
(59) Ichikawa, T. Electron Diffraction Study of the Local Atomic Arrangement in Amorphous Iron and Nickel Films. *Phys. status solidi (a)* **1973**, *19* (2), 707−716.
(60) Gupta, P. K. Non-Crystalline Solids: Glasses and Amorphous Solids. *J. Non-Cryst. Solids* **1996**, *195* (1−2), 158−164.
(61) Dreyer, A.; Eckstädt, K.; Koop, T.; Jutzi, P.; Hütten, A. Surface Stabilization Determines a Classical versus Non-Classical Nucleation Pathway during Particle Formation. *RSC Adv.* **2016**, *6* (78), 74061−74066.
(62) Lefky, C.; Mamidanna, A.; Huang, Y.; Hildreth, O. Impact of Solvent Selection and Temperature on Porosity and Resistance of Printed Self-reducing Silver Inks. *Phys. status solidi (a)* **2016**, *213* (10), 2751−2758.

https://doi.org/10.1021/acsanm.4c05047
ACS Appl. Nano Mater. XXXX, XXX, XXX−XXX

(63) Kappert, E. J.; Pavlenko, D.; Malzbender, J.; Nijmeijer, A.; Benes, N. E.; Tsai, P. A. Formation and Prevention of Fractures in Sol−Gel-Derived Thin Films. *Soft Matter* **2015**, *11* (5), 882−888.
(64) Singh, K. B.; Tirumkudulu, M. S. Cracking in Drying Colloidal Films. *Phys. Rev. Lett.* **2007**, *98* (21), No. 218302.
(65) Galliker, P.; Schneider, J.; Eghlidi, H.; Kress, S.; Sandoghdar, V.; Poulikakos, D. Direct Printing of Nanostructures by Electrostatic Autofocussing of Ink Nanodroplets. *Nat. Commun.* **2012**, *3* (1), 890.
(66) Nydegger, M.; Pruška, A.; Galinski, H.; Zenobi, R.; Reiser, A.; Spolenak, R. Additive Manufacturing of Zn with Submicron Resolution and Its Conversion into Zn/ZnO Core−Shell Structures. *Nanoscale* **2022**, *14* (46), 17418−17427.
(67) Grinstaff, M. W.; Salamon, M. B.; Suslick, K. S. Magnetic Properties of Amorphous Iron. *Phys. Rev. B* **1993**, *48* (1), 269−273.
(68) Mohapatra, J.; Liu, X.; Joshi, P.; Liu, J. P. Hard and Semi-Hard Fe-Based Magnetic Materials. *J. Alloy. Compd.* **2023**, *955*, No. 170258.
(69) Nix, W. D.; Gao, H. Indentation Size Effects in Crystalline Materials: A Law for Strain Gradient Plasticity. *J. Mech. Phys. Solids* **1998**, *46* (3), 411−425.
(70) Ramamurty, U.; Jana, S.; Kawamura, Y.; Chattopadhyay, K. Hardness and Plastic Deformation in a Bulk Metallic Glass. *Acta Mater.* **2005**, *53* (3), 705−717.

https://doi.org/10.1021/acsanm.4c05047
ACS Appl. Nano Mater. XXXX, XXX, XXX−XXX